J. Fluid Mech. (2008), *vol.* 598, *pp.* 121–139.
doi:10.1017/S0022112007009937 Printed in the United Kingdom

Experimental study of higher-order moments in shear-driven boundary layers with rotation

E. FERRERO[1], R. GENOVESE[2,3,4], A. LONGHETTO[3],
M. MANFRIN[3] AND L. MORTARINI[1]

[1]Dip. di Scienze e Tecnologie Avanzate, Università del Piemonte Orientale, via Bellini 25/g,
15100, Alessandria, Italy
enrico.ferrero@mfn.unipmn.it

[2]Centro E. Fermi, Compendio Viminale, 00184, Roma, Italy

[3]Dip. di Fisica Generale, Università di Torino, via Pietro Giuria 1, 10125, Torino, Italy

[4]Politecnico di Torino, Corso Duca degli Abruzzi 24, 10129, Torino, Italy

(Received 23 March 2007 and in revised form 30 October 2007)

The results of laboratory wall turbulence experiments on a shear-driven rotating boundary layer are presented. The experiments were carried out in the Turin University Laboratory rotating water tank. The flow was generated by changing the rotation speed of the platform and measured by means of particle image velocimetry. In order to analyse the influence of the rotation and of surface roughness, different cases were examined. Several rotation periods were considered. The measurements were performed both over a smooth surface and over a rough-to-smooth transition. Mean flows and the higher-order moments of the velocity probability density function are shown and discussed together with a comparison of the different experimental cases, theory and large-eddy simulations.

1. Introduction

The aim of this work is to investigate the higher order moments (HOMs) in a neutral, shear-driven, rotating boundary layer. This is a topic of great interest in many research fields such as fluid dynamics, atmospheric physics, astrophysics, and oceanography. The shear-driven boundary layer has been studied from many points of view both experimentally and theoretically. The experimental works include both field and laboratory measurements. In particular, the possibility of easily changing the values of the external governing parameters of the boundary layer and the boundary conditions makes the latter a useful tool for investigations.

Second- and third-order moments were theoretically investigated by Hunt & Carlotti (2001). In that paper the statistical structure in the surface layer at the wall was studied and the presence of an eddy surface layer, where an internal boundary layer (IBL) can develop, was shown.

Experimental measurements were performed by Drobinski *et al.* (2004) who analysed sonic anemometers, rawinsondes and Doppler Lidar data to investigate the layered structure of the surface layer and to provide observational evidence of the eddy surface layer. In a second paper (Drobinski *et al.* 2007) they showed the different nature of turbulence near the wall in terms of organized eddies, velocity fluctuation spectra and second-order moments statistics, comparing measurements and LES data. The structure of the turbulent boundary layer, in near-neutral conditions, was studied by Grant (1986, 1992) carrying out field experiments, while measurements from aircraft over the sea were performed by Nicholls & Readings (1979).

Among numerical models, Moeng & Sullivan (1994) presented numerical large-eddy simulation (LES) results of the second- and third-order moments of atmospheric turbulence under the Earth's Coriolis effect. The structures that developed in a neutrally stratified boundary layer were investigated by Lin *et al.* (1996) by analysing turbulent kinetic energy, momentum fluxes and vorticity fields in LES accounting for the Coriolis force and roughness.

The boundary layer turbulent structure is shown by the turbulence HOMs which are crucial for investigating its non-local nature (Zilitinkevich *et al.* 1999; Ferrero & Racca 2004) and for estimating the departure of the velocity probability density function (PDF) from the widely used Gaussian (quasi-normal, QN) approximation (Monin & Yaglom 1971; Hanjalic & Launder 1972, 1976; Zeman 1981). It should be mentioned that the QN approximation was recently criticized and some attempts to overcome its limitations (namely the unphysical growth of the third-order moments and the moment oscillation in the stable layer) have been made (Cheng, Canuto & Howard 2005; Gryanik & Hartmann 2005).

The importance of the determination of the HOMs is highlighted through the need to compare recently developed numerical models based on the averaged Reynolds stresses (Ferrero 2005; Cheng *et al.* 2005) and measured profiles. Field experiments provide some data sets, but, due to the estimation problems, they rarely include higher-order statistics, up to the fourth order (Hartmann *et al.* 1999), and the comparison with model data is generally difficult (Qian *et al.* 2000). These data are usually obtained by wind tunnel experiments (Khurshudyan, Snyder & Nekrasov 1981, Ohba *et al.* 2002), that do not generally include the rotation effects, or from LES (Moeng & Sullivan 1994; Rizza *et al.* 2003) and direct numerical simulations (DNS) (Mason & Thomson 1987; Coleman, Ferzinger & Spalart 1990).

In this paper the HOMs behaviour is analysed by focusing on two key aspects: the effects of rotation of the reference frame and the influence of an heterogeneous surface on the wall-normal structure of the near-wall boundary layer. Coriolis forces are usually investigated in atmospheric topics, but they are also pertinent to theoretical fluid dynamic aspects.

Extended reviews of the dynamics connected to rotation have been given by Bidokhti & Tritton (1992), who reported laboratory experiments on the turbulence development, and structure in the free shear layer (Pedlosky 1987; Tritton 1988).

In a previous work (Ferrero *et al.* 2005), our group studied the boundary layer developed in a rotating reference frame ('Coriolis' turntable) restricting the analysis to the second-order moments of turbulence. We concentrated our attention on the similarities with an atmospheric boundary layer but did not modify the tank revolution time.

In this paper a shear-driven boundary layer was created in the Turin University Rotating Laboratory (TURLab) of the Department of General Physics water tank. The roles played by the rotation and by the transition from a rough to smooth wall in the development of organized turbulent structures which are responsible for the non-local transport are investigated by analysing the turbulent statistics and in particular the HOMs.

Turbulence statistics are compared with numerical data, disregarding the possible differences arising from the streamline curvature present in our laboratory experiments. This limitation in the comparison might explain some of the discrepancies found.

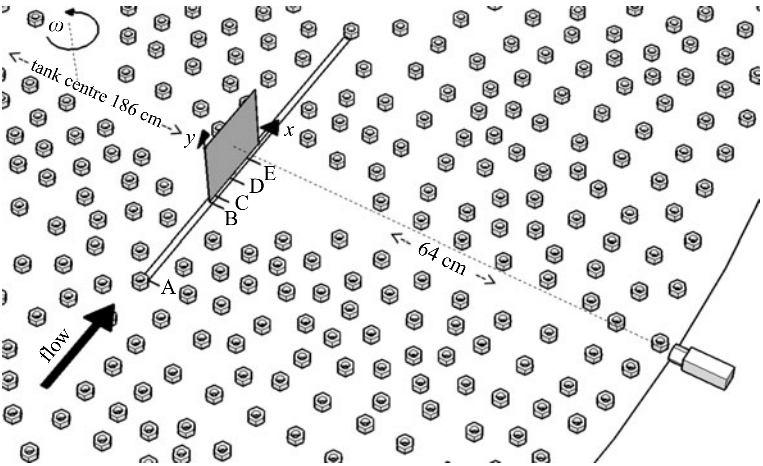

FIGURE 1. Experimental setup: measurement field (laser sheet) (shown in grey) and roughness element placements. B indicates the measurement field edge and C, D and E are the locations where the profiles were evaluated. The black arrow shows the flow direction outside the Ekman layer.

In § 2 the PIV technique, the experimental apparatus and the instrumentation are presented, while, in § 3, results of the experiments are presented and discussed through comparison with theoretical and numerical previous findings. Finally, in § 4, the main results and conclusions are summarized.

2. The laboratory experiment

2.1. *PIV measurements*

The laboratory experiments took place at the TURLab using a hydrodynamic rotating tank. The facility is composed of a 5 m diameter cylindrical tank, able to reach a maximum rotation speed of 20 revolutions per minute. The data were acquired by a non-intrusive PIV technique which allows the detection of Eulerian velocity fields.

The presented experiments were carried out by spreading passive tracers in the water inside the tank, lit by a light sheet produced by a green diode laser coupled with a beam expanding optical device, while a high-resolution digital camera recorded snapshot sequences of the flow at adjustable time rates. The diameter of the passive tracers was 30 μm, the water depth 40 cm and the camera frame rate 107.6 Hz (except for case 1B where it was 269.0 Hz). To avoid reflection problems, the laser sheet came directly out from an optical crystal located inside the tank bottom (see figure 1).

The flow was analysed on a rectangular grid of about $10 \times 8\,\mathrm{cm}^2$. Most of the images were sufficiently good to allow the use of a rectangular interrogation window of about 30×20 pixels, giving a final resolution of about 60×80 vectors (the exact number changes slightly in the different experiments, due to small differences in the camera view fields).

2.2. *Experimental setup*

Since we were interested in the effect of both rotation and surface roughness on the boundary layer development, the shear effects were evaluated for two different configurations of the tank floor: a flat smooth wall and a rough area followed by a smooth surface (rough-to-smooth). This second condition was obtained by gluing

Exp.	Surface	Re_δ	Re_f	$U_0\,(\mathrm{cm\,s^{-1}})$	u_τ $(\mathrm{cm\ s^{-1}})$	δ (cm)	T_1(s)	Ro_δ
case 0	smooth	5390	550	9.8	0.5	5.5	100	0.7

TABLE 1. Estimated parameters for the basic case.

plastic roughness elements on the tank floor before and around the measurement region, as shown in figure 1. Each element was 2 cm wide, 1.2 cm high and the mean distance between the elements was about 4 cm. The laser sheet was in a plane normal both to the tank bottom at a distance of 186 cm from the centre and to the radius along the camera axis. For the laser sheet exit, an area 1 cm wide and 50 cm long, corresponding to the window through which the laser sheet shone, was left free of roughness elements. As shown in figure 1 an area about 10 cm wide in front of the laser sheet was also left free from roughness elements in order to allow the camera view of the measurement sections and to avoid laser reflections. Hence, even though, in the Ekman layer the flow was not strictly azimuthal but an inward component develops, in the rough-to-smooth case, this crossflow was not influenced by the roughness elements surrounding the measurement area.

In the following, we will take x and y as the downstream tangential wall-parallel and the cross-stream wall-normal directions respectively.

A mean flow $U(r)$ at the distance r from the centre of the tank can be created by changing the tank rotation speed as described by Ferrero *et al.* (2005). The laser sheet was placed tangential to the tank circumference and hence it was aligned with the mean flow outside the boundary layer. This is the flow component we measured. We performed a series of experiments with different velocities (obtained by choosing different values for the initial (T_0) and final (T_1) rotation periods).

A first experiment was carried out over the smooth surface and with a relatively small rotation ($T_1 = 100$ s) in order to compare it not only with the classical boundary layer theory, but also with some previous experimental works and numerical simulations (Adrian, Meinhart & Tokins 2000), (Coleman *et al.* 1990; Moeng & Sullivan 1994).

The angular velocity of the tank was changed in the next two experiments (rotation periods: $T_1 = 40$ s for case 1A and $T_1 = 10$ s for case 1B), while the surface configuration was left unchanged. Then, in cases 2A and 2B the rotation period was kept constant while the surface configuration was modified, case 2A: was for a smooth surface and case 2B for a heterogeneous surface. The aim of this analysis is to compare two cases which differ only in the rotation and two cases which differ only in the surface roughness.

The main parameters for the different experiments are summarized in tables 1, 2 and 3.

2.3. *PIV analysis*

The PIV software identifies the displacements of clustered seeding elements through cross-correlation techniques, and then evaluates the flow velocity field in the monitored region (Fincham & Spedding 1997; Bernero & Fiedler 2000): the experiments produce a time series of images of the fluid, which are cross-correlated pair by pair to obtain the displacements of particle patches over a sufficiently small time interval and spatial domain (Raffel, Willert & Kompenhans 1998).

Exp.	Surface	Re_δ	Re_f	U_0 (cm s^{-1})	u_τ (cm s^{-1})	δ (cm)	T_1 (s)	Ro_δ
case 1A	smooth	1120	230	6.4	0.23	2.6	40	0.4
case 1B	smooth	1120	110	6.4	0.28	2.8	10	0.1

TABLE 2. Estimated parameters for the two cases over the same surface with different rotation velocity.

Exp.	Surface	Re_δ	Re_f	U_0 (cm s^{-1})	u_τ (cm s^{-1})	δ (cm)	T_1 (s)	Ro_δ
case 2A	smooth	3115	500	8.8	0.5	3.5	100	1.1
case 2B (0.5 h_r)	sm-to-rough	6090	490	8.8	1.1	7.0	100	1.3
case 2B (3.5 h_r)	sm-to-rough	6090	490	8.8	0.8	7.0	100	0.9
case 2B (6.6 h_r)	sm-to-rough	6090	490	8.8	0.7	7.0	100	0.8

TABLE 3. Estimated parameters for the two cases over different surfaces with the same rotation velocity.

Thereafter, the correlation image velocimetry (CIV) algorithm (Fincham & Spedding 1997) is applied to calculate the two-dimensional velocity vectors on an irregular planar grid. To achieve accurate velocity values, CIV results need to be filtered to remove bad vectors; the filtering operations are performed step by step, starting from a scatter analysis of the velocity distribution, and then using local mean/median algorithms developed at the TURLab. A final patch procedure has to be applied to compute the vector field over a regular grid.

Following Adrian *et al.* (2000), we verified that the ratio between the particle image size and the pixel size was greater than 4 (Prasad *et al.* 1992). The maximum value over all the experiments considered here was about 12. In this case the uncertainty of the measurements is roughly from one-tenth to one-twentieth of the particle-image diameter. Dividing these values by the mean particles displacement, the relative error in the velocity can be obtained. In our case we found about 6 %, which coincides with the values found by Tarbouriech, Didelle & Renouard (1997) for a PIV system developed, like the one used in our experiments, from Fincham & Spedding (1997). Note that the maximum size of the particles images (12 pixels) does not correspond to the size of the particle itself, but owing to its movement and to the exposure time during the acquisition, it can appear longer than if it were at rest in the flow direction (as a short streak). This value corresponds to the maximum length in the free shear layer, while the particle width was always about 5 pixels. In the turbulent layer the particle-image size was about 5×5 pixels.

In order to carry out a statistical description of the flow we acquired 1400 images with a time interval of 9×10^{-3} s (except for case 1B where it was 4×10^{-3} s), so the total group of images corresponded to a time interval of 12.6 s (5.6 s for case 1B). For calculating the profiles of the turbulence moments presented here, we considered every pair of images as an element of the statistical sample made up of 1400 factors (every image is part of two pairs) and computed the mean over the whole ensemble of 1400 fields. The data stationarity was checked with a test run (Bendat & Piersol 1986) with a significativity level of 5 %.

The profiles of the mean flow and turbulence moments were obtained by averaging both in time and space (about 70×1400 grids points), except for the case of non-homogenous surface for which only time average was applied. Note that the flow is homogeneous in a plane parallel to the bottom wall in the smooth cases, whilst in the rough-to-smooth one the assumption of homogeneity cannot be made for the whole domain in the downstream direction, where flow adjustment and internal boundary layer development are expected (Rao, Wyngaard & Coté 1973). Therefore, the spatial mean in the downstream direction was not computed. The average is indicated by the symbol $\langle \cdot \rangle$.

The high frequency of the PIV system allows the small-scale turbulence to be resolved. The convergence of the moments has been verified following Lenschow, Mann & Kristensen (1994), who demonstrated that it depends on the ratio between the integral time scale and the sample time. In our experiments the integral time scale (evaluated according to Gluhovsky & Agee (1994)) varies from 0.03 s to 0.2 s, which corresponds to a ratio with the sample time of 0.006 and 0.015 respectively. Our choice of the sample time length was the best compromise among three factors: it should be short enough to guarantee the stationarity of the data and not exceed the memory of the acquisition storage, and at the same time be as long as possible to ensure the HOMs convergence.

3. Results

First, the characteristic parameters of the boundary layer, namely friction velocity u_τ and boundary layer height δ, were evaluated. The friction velocity u_τ was estimated as the square root of the maximum value of the total shear stress given by the turbulent and the viscous stress summation:

$$u_\tau = \sqrt{\left(-\langle u'v' \rangle + \nu \frac{\partial U}{\partial y}\right)}, \tag{3.1}$$

where $u = U + u'$, $v = V + v'$, upper case indicating mean values and primes the fluctuations $\lambda; \nu$ is the kinematic viscosity. Since we only measured the wall-parallel (u) and wall-normal (v) components of the velocity fields, the turbulent kinetic energy k was estimated by assuming the variance of the spanwise component equal to one half of $\langle u'^2 \rangle$ (Drobinski *et al.* 2004), then boundary layer depth δ was deduced as the height at which k vanishes:

$$k = \tfrac{1}{2}(\langle u'^2 \rangle + 0.5\langle u'^2 \rangle + \langle v'^2 \rangle). \tag{3.2}$$

In tables 1, 2 and 3, the estimated parameters (u_τ, δ) for the five cases considered are summarized together with the asymptotic velocity U_0, the final rotation period T_1, the Reynolds numbers Re_δ and Re_f, and the Rossby number $Ro_\delta = \delta_f/\delta$, defined as the ratio between the scale of the rotating turbulent boundary layer $\delta_f = u_\tau/f$ and boundary layer thickness δ. The first column in table 3 also reports, for case 2B, the distance (point C, D or E in figure 1) from the measurement field edge in terms of the roughness element height $h_r = 1.2\,\text{cm}$.

For comparison two different Reynolds numbers were estimated, Re_δ and Re_f (Coleman *et al.* 1990), using two length scales. $Re_\delta = u_\tau \delta/\nu$ takes the boundary layer depth δ as a length scale, and consequently indicates how the turbulence generated by the shear of the mean flow develops. On the other hand, $Re_f = U_0/(\frac{1}{2}\nu f)^{1/2}$ takes into account the Ekman layer depth $\sqrt{2\nu/f}$, showing the role of the rotation in the turbulence development.

The measurements were performed during the velocity decay after an abrupt change of rotation; the characteristic time scale of this decay was much longer than the measurement time. We verified the data stationarity with an approprate test, as

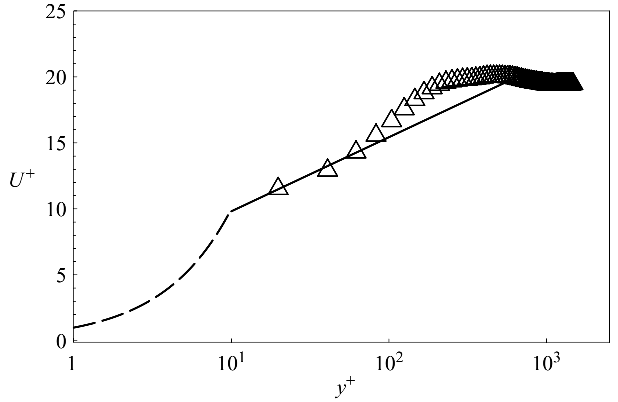

FIGURE 2. Normalized mean velocity vs. normalized wall distance. △, measurements; solid line, log-law for $y^+ > 10$; dashed line, $U^+ = y^+$ for $y^+ < 10$.

previously described above. In cases 0, 2A and 2B, the tank was spun down while 1A and 1B correspond to a spin up. The initial periods were 162 s (case 1A), 104.5 s (case 1B), 35 s (case 2A), 35.5 s (case 2B), 35 s (case 0); the duration of the rotation velocity change was of the order of a few seconds; the delay between the change and the aquisition was between 500 s and about 1000 s. The distance of the measurament plane from the rotation axis was 1.86 m. Finally, the mean velocity decreases during the acquisition by about 1 % (except for the rough-to-smooth case 2B in which was about 3 %) without violating the stationarity (see § 2.3).

3.1. *Basic case*

First, an experiment at low rotation speed ($T_1 = 100$ s) (case 0) was carried out in order to verify the consistency of our measurements with the boundary layer theory and other previous works. The effect of the streamline curvature was disregarded. Hence the measurement results are compared with literature data where the streamline curvature effect is not present.

In figure 2 a comparison between U^+, the measured mean velocity normalized with u_τ, as a function of the normalized distance $y^+ = yu_\tau/\nu$, and the log-law (Millikan 1938) is shown. For comparison the line $U^+ = y^+$ is also shown, although no data are available for $y^+ < 10$. Unfortunately, close to the wall a layer of high particle concentration reflects the laser sheet in the glass and prevents the PIV analysis in this region.

The measured profile agrees with the log-law, which is derived for a non-rotating boundary layer, in a layer between $y^+ = 10$ and $y^+ = 10^2$, then it departs from the theoretical law showing the overshoot due to the Ekman layer.

The log-law applies in a layer whose depth is reduced by the rotation as observed by Coleman *et al.* (1990). The best fit of the data is obtained with the following log-law:

$$\frac{U(y)}{u_\tau} = \frac{1}{k_v} \ln \frac{yu_\tau}{\nu} + B \tag{3.3}$$

where the constant $B = 4.2$ is within the values previously found in the literature $3.5 < B < 6.1$ (Zanoun, Durst & Nagib 2003), and $k_v = 0.4$ is the von Kármán constant.

Case 0 was assumed to be the close to the reference LES case of Moeng & Sullivan (1994), even through the Rossby number was one tenth of that of the LES. However a

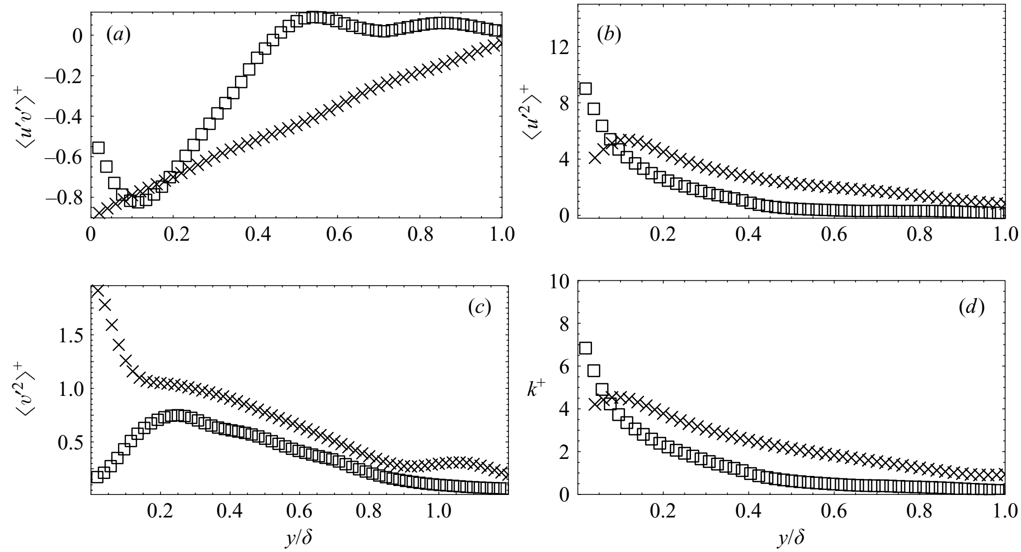

FIGURE 3. Case 0: normalized SOMs vs. normalized wall distance. □, measurements; ×, LES data.

comparison with the LES profiles confirms that the effect of the rotation was similar in the two (simulated and measured) cases. Further the Rossby number for case 0 was of the order of one, hence the boundary layer and rotation based heights were very similar suggesting that the influence of the rotation on the boundary layer turbulence was negligible. This Rossby number value can be considered as a critical value for the rotation. In the other cases (1A and 1B), characterized by different rotations, the Rossby number reduces by about one half or more, suggesting the influence of the rotation on the developed turbulence.

Figure 3(*a*–*d*) show the velocity fluctuation second-order moments (SOMs) profiles, normalized with u_τ^2, as a function of the wall distance, normalized with the boundary layer depth δ. It can be observed that their trends qualitatively agree with the profiles from Adrian *et al.* (2000) in a non-rotating laboratory experiment and with the results of rotating numerical experiments carried out by Coleman *et al.* (1990), both at low Reynolds numbers. In figure 3 the results of the LES by Moeng & Sullivan (1994) are also shown for comparison. Both wall-normal and wall-parallel variances show measured values similar to those of the LES in the whole boundary layer except in the proximity of the wall ($\delta < 0.1$) where the subgrid-scale (SGS) model of the LES is dominant in resolving the small-scale features. Considering the discussion by Drobinski *et al.* (2004, 2007) on the contribution of Moeng & Sullivan's (1994) SGS scheme to their vertical velocity variance, the SGS model seems to dominate up to about 0.1δ only. However, the numerical simulation performed by Ferrero (2005), using a third-order model, suggests that discrepancies between higher-order closure and the SGS model can be found up to about 0.2δ.

Furthermore the LES refers to an atmospheric boundary layer, characterized by a Reynolds number much higher than those of our experiment. On the other hand the Rossby number $Ro_\delta = \delta_f/\delta$ in the LES case ($Ro_\delta = 10$) is just an order of magnitude bigger than in our laboratory experiment ($Ro_\delta = 0.7$).

Concerning the streamwise shear stress (figure 3*a*), it can be observed that the measured values decrease more rapidly with the distance from the wall, reaching zero

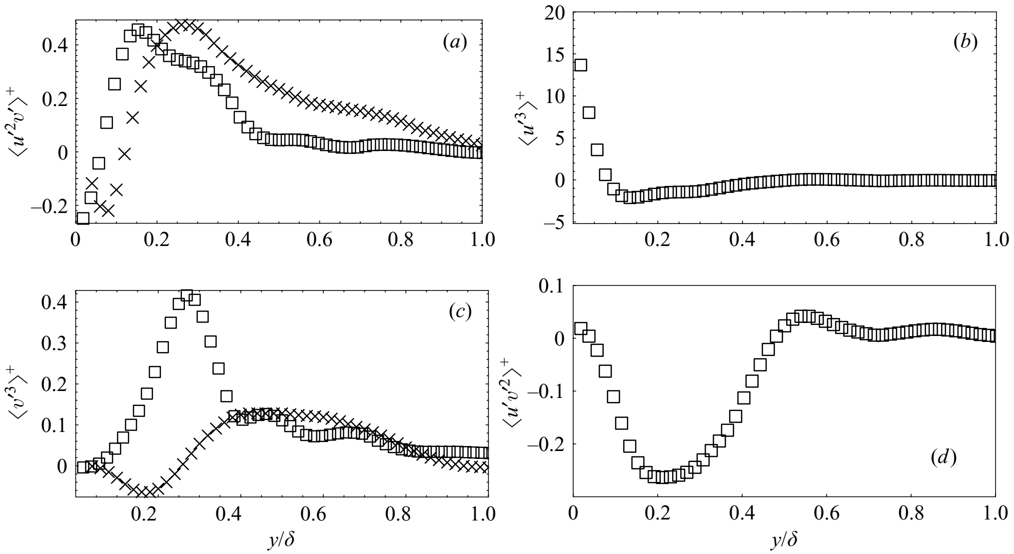

FIGURE 4. Case 0: normalized TOMs vs. normalized wall distance. □, measurements; ×, LES data.

at about 0.5δ. This can be related to the Rossby number in the experiment being smaller than in the LES. The higher rotation, which is characterized by lower Rossby number, reduces the streamwise momentum flux at large distances, while the spanwise shear production could probably become dominant, explaining the turbulent kinetic energy production up to δ.

Another aim of this work is to investigate the presence of instabilities that can develop and give rise to large organized structures, through the third-order moments (TOMs) analysis. Such structures are also responsible for the turbulent non-local transport which can be described by the TOMs of the velocity PDF. As is well known, in turbulence models the non-local transport is described through the TOMs, which can be thought as the fluxes of fluxes (Zilitinkevich *et al.* 1999). Hence, the large departure of TOMs from the Gaussian value (which is zero) corresponds to the effect due to the large structures possibly present in the boundary layer.

Ferrero & Racca (2004) recently showed that to correctly predict the boundary layer depth in neutral shear-driven turbulence the TOMs have to be taken into account. For these reasons, in order to improve the investigation of the boundary layer developed in the laboratory, the TOMs of the turbulent velocity PDF were also calculated.

In figure 4(*a–d*) the profiles of the TOMs (normalized with u_τ^3) are depicted as a function of the normalized distance (y/δ). The LES data available in Moeng & Sullivan (1994) are also reported for the moments. The results of the comparison demonstrate that the LES data for the TOMs, are compatible with those of the experiment. Only the $\langle v'^3 \rangle$ profile shows some discrepancies in a layer close to the wall. However it should be emphasized that the LES results can be considered for comparison with TOMs only in the layer where the size of the eddies is large enough to be resolved by the model grid. In the proximity of the wall, where the turbulence scale is smaller, the TOMs cannot include the SGS model contribution, because it adopts a second-order closure, and hence shows an erroneous behaviour for the HOMs (Moeng & Sullivan 1994). These discrepancies in some cases appear for distances greater than 0.1 δ, the value suggested by Drobinski *et al.* (2004, 2007). However similar differences were found by Ferrero (2005).

All the TOMs show non-negligible values from the wall up to about one half of the boudary layer thickness, except for $\langle u'^3\rangle$, which shows very high values only in a thin layer close to the wall. Consequently wall-normal transport of turbulence is present in the whole boundary layer, due probably to large-scale structures which, as found in previous works, can develop not only in stratified flows but also in purely shear-driven boundary layers (Adrian *et al.* 2000; Ferrero & Racca 2004; Drobinski *et al.* 2004).

The nature of these structures, which depends on the Reynolds number, is not yet clearly understood. In boundary layers simulated in non-rotating wind tunnels they are known as horseshoes or hairpins (Adrian *et al.* 2000), while in large-scale flows such as geophysical flows, they are called streaks or rolls (Drobinski *et al.* 2004; Moeng & Sullivan 1994).

For low Reynolds numbers Coleman *et al.* (1990) demonstrated with a DNS the presence of longitudinal roll vortices in a shear-driven boundary layer. On the other hand, Mason & Sykes (1980) were able to find roll-like eddies in a two-dimensional simulation with a finite-difference model of the Boussinesq equations but Mason & Thomson's (1987) (three-dimensional) LES did not confirm their presence.

Thanks to our PIV system we can calculate up to the fourth-order moments (FOMs). Besides being useful in the determination of the shape of the velocity PDF, these quantities are particularly interesting because they allow one to assess and to check the validity of the well-known quasi-normal (QN) approximation (Hanjalic & Launder 1972, 1976; Zeman 1981) based on the Millionshchikov Hypothesis (Monin & Yaglom 1971) and considered in the eddy-damped quasi-normal Markovian (EDQNM) approximation (Lesieur 1997), widely adopted in turbulence models to close the FOMs (Canuto 1992; Ferrero 2005). This approximation postulates that the FOMs can be expressed as a combination of the second-order moments assuming a Gaussian distribution:

$$\langle a'b'c'd'\rangle = \langle a'b'\rangle\langle c'd'\rangle + \langle a'c'\rangle\langle b'd'\rangle + \langle a'd'\rangle\langle b'c'\rangle \qquad (3.4)$$

Unfortunately, FOM measurements are not usually available with enough precision to evaluate small departures from the QN approximation.

In figure 5 the FOMs, normalized with u_τ^4 are shown toghether with the corresponding moments given by the QN approximation. It can be observed that the FOMs generally agree with the QN approximation profiles, although some discrepancies appear.

3.2. *Rotation effect*

In order to assess how the rotation can modify the flow structure, regarding the mean velocity and the turbulence, we carried out a series of experiments at higher rotation speed. We show here a comparison between two cases characterized by a rotation period of 40 s (1A) and 10 s (1B) (table 2).

In figure 6 the normalized mean velocity ($U^+ = U/u_\tau$), as a function of the normalized distance from the wall ($y^+ = yu_\tau/\nu$), is depicted for the two rotation speeds. The discrepancies in the asymptotic values depend on the differences in u_τ generated by the rotation. The typical overshooting characteristic of the Ekman layer can be observed.

The normalized shear stress, the streamwise and the wall-normal variances, and the resulting turbulent kinetic energy k (normalized with u_τ^2) are shown in figure 7(*a*–*d*).

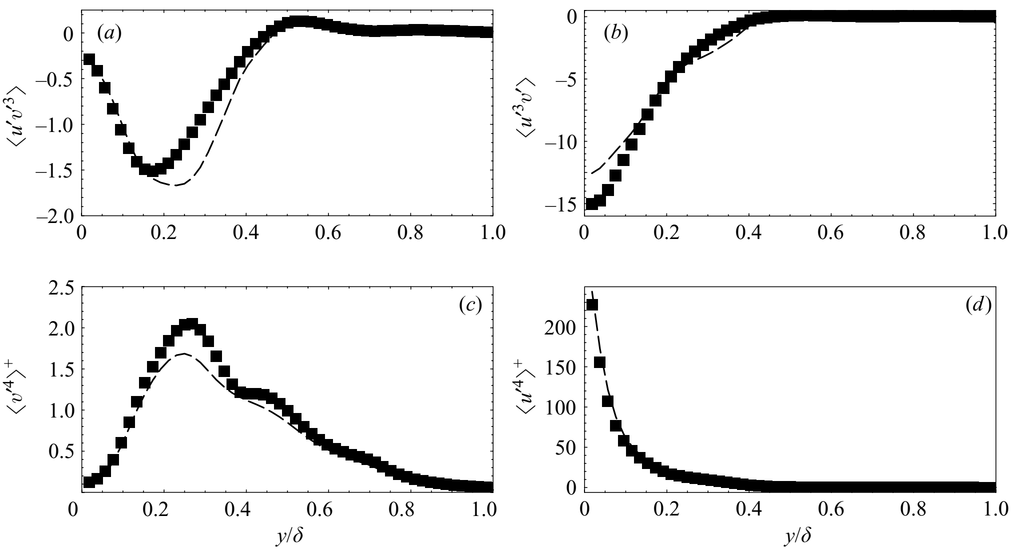

FIGURE 5. Case 0: normalized FOMs vs. normalized wall distance. ■, measured data; dashed line: QN approximation.

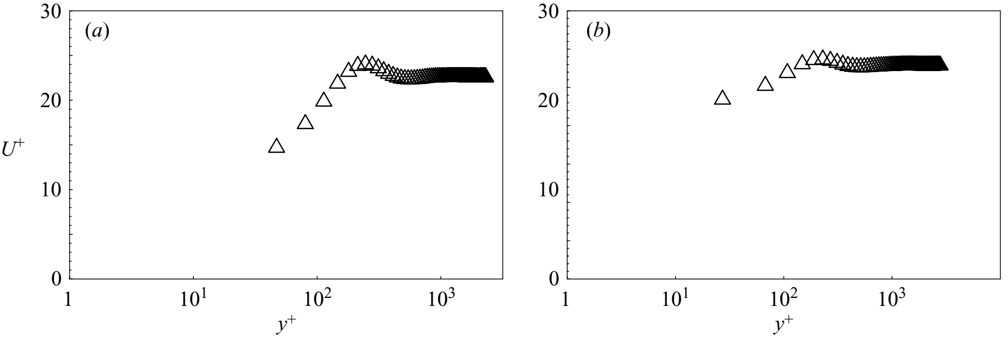

FIGURE 6. Case 1: normalized mean velocity vs. normalized wall distance. (*a*) $T_1 = 40$ s; (*b*) $T_1 = 10$ s.

All moment profiles are consistent with the previous, slow rotating, case and LES data, but, the influence of the faster rotation can be observed. The shear stress trends show similar behaviour in the two cases. They reach a maximum (negative) value at different distances from the wall, which decreases with the rotation period.

The value of $\langle u'^2 \rangle$ is higher in the case 1B close to the wall, and it decreases more rapidly with the distance than case 1A.

The profile of $\langle v'^2 \rangle$ presents a maximum at about one half of the boundary layer height in case 1A and at about 0.3 δ, when the rotation period reduces in case 1B.

The magnitude of the streamwise variance is larger than the wall-normal one, hence the behaviour of k reproduces that of $\langle u'^2 \rangle$ one, as can be observed in figure 7 (*d*).

In conclusion, the increasing rotation speed seems to make the turbulent layer shallower and to reduce the distance at which the turbulent moments attain their maximum value. Turbulence develops in a deeper layer if the rotation speed is slower and shows higher intensity close to the wall for faster rotation.

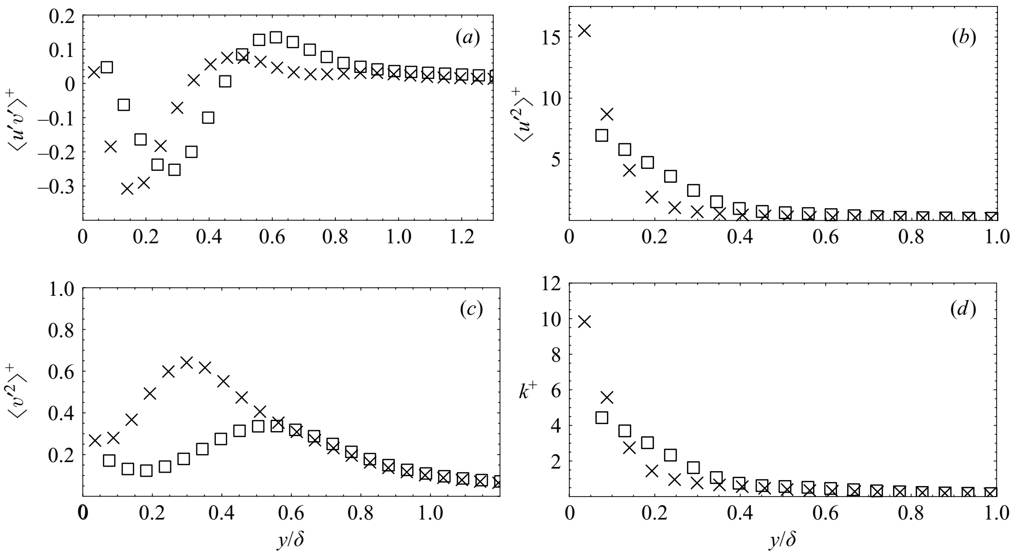

FIGURE 7. Case 1: normalized SOMs vs. normalized wall distance. □, case 1A, ×, case 1B.

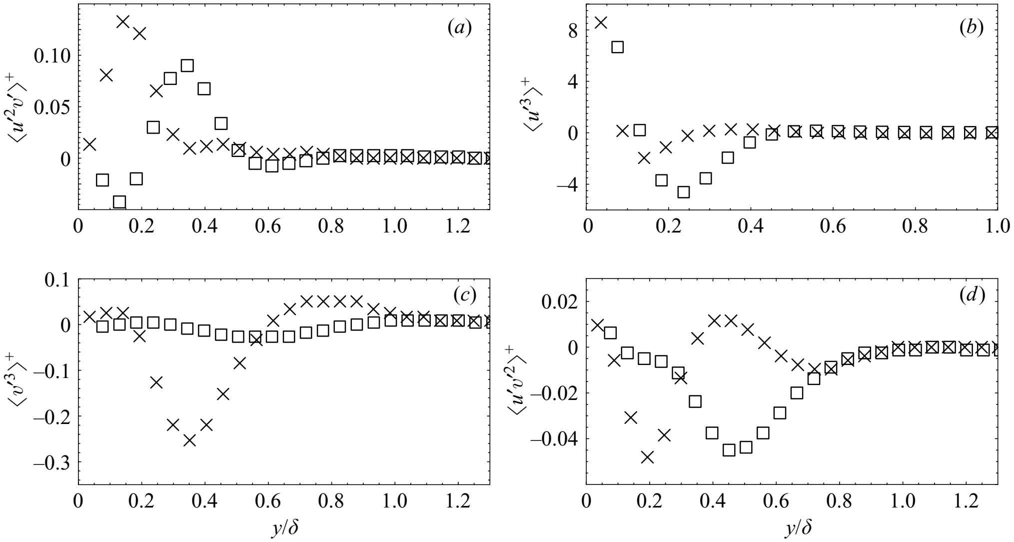

FIGURE 8. Case 1: normalized TOMs vs. normalized wall distance. □, case 1A, ×, case 1B.

TOMs (normalized with u_τ^3) measured for cases 1A and 1B are depicted in figure 8(*a*–*d*). The general behaviour is similar to case 0, though some discrepancies appear. Differences are also found between cases 1A and 1B. The positions of maxima are observed to be located farther away for slower rotation speed, as in case 1A, which shows a deeper turbulent layer. As TOMs are related to the turbulent transport, this means that organized structures develop more in a boundary layer characterized by slight rotation. There is an unexpected negative maximum $\langle v'^3 \rangle$, more pronounced in case 1B, indicating a counter-gradient region.

The FOMs and QN approximation (normalized with u_τ^4) for experiments 1A and 1B (figure 9*a*–*d*) demonstrate that, in the case of faster rotation speed, the

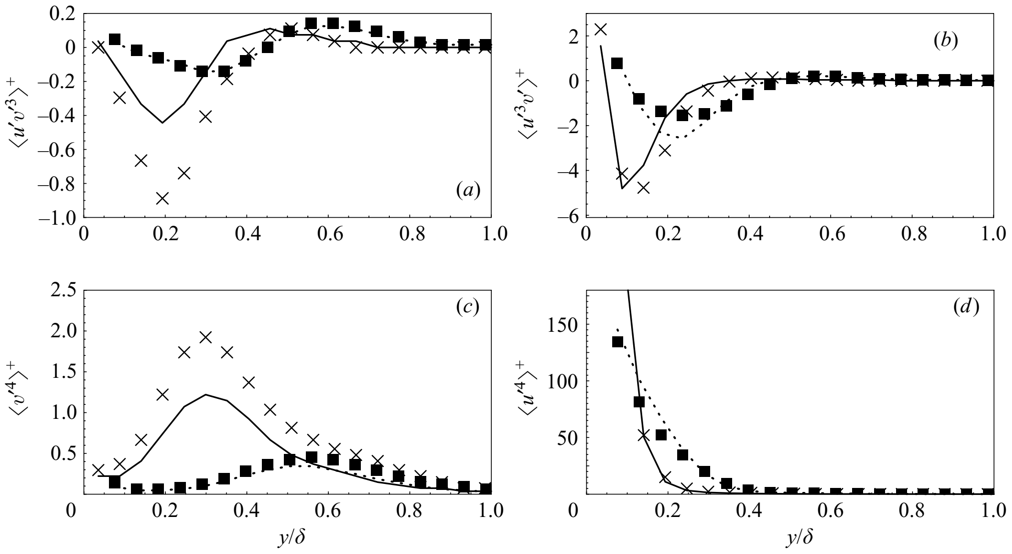

FIGURE 9. Case 1: normalized FOMs vs. normalized wall distance. ■, case 1A and ×, case 1B. The dotted line is the QN approximation for case 1A, the solid line is the QN approximation for case 1B.

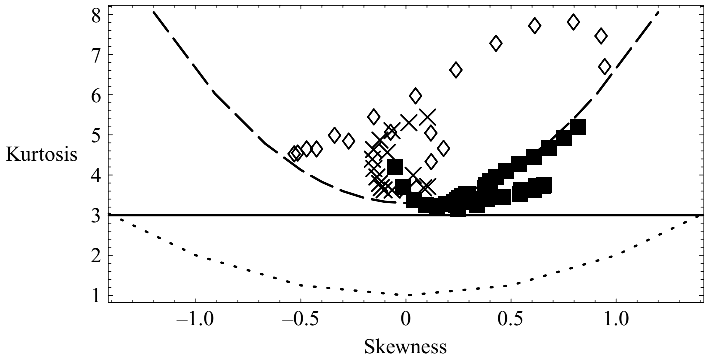

FIGURE 10. Kurtosis as a function of the skewness for cases over the smooth surface. ■, case 0; ×, case 1A; ◇, case 1B. Dashed line: $Ku = 3.3(S^2 + 1)$, solid line: $Ku = 3$; dotted line: $Ku = S^2 + 1$.

QN hypothesis is not able to reproduce the exact behaviour of the measured moments, underestimating the FOM profiles, as also found in atmospheric (Gryanik & Hartmann 2005) and oceanic (Losch 2004) flows, with the exception of the $\langle u'^4\rangle$ profile. The agreement is less satisfactory when the rotation speed increases, thus showing that the rotation modifies the PDF of the velocity fluctuations.

In figure 10 the kurtosis (Ku) of the normal velocity component v' is depicted as a function of its skewness (S). It can be seen that the values measured in cases 1A and 1B are above the curve corresponding to the relation found by Tampieri, Maurizi & Alberghi (2000) for sheared flow:

$$Ku = 3.3(S^2 + 1) \tag{3.5}$$

and above the curve corresponding to the statistical limit $Ku \geqslant (S^2 + 1)$.

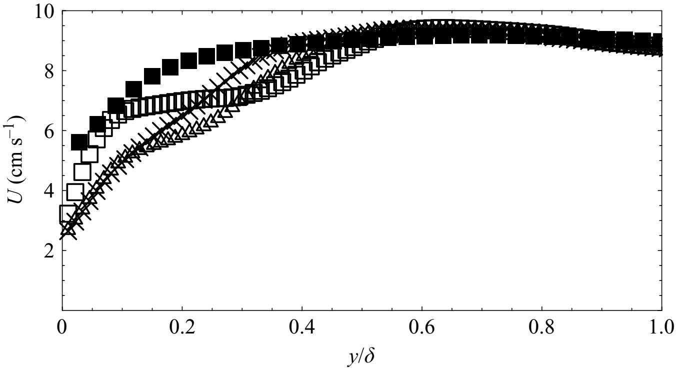

FIGURE 11. Case 2: mean velocity vs. normalized wall distance. ■, case 2A; ×, case 2B (0.5 h_r); △, case 2B (3.5 h_r); □, case 2B (6.6 h_r).

Equation (3.5) was found by fitting the relation $Ku = \alpha(S^2 + 1)$ with the vertical velocity component measured in the laboratory, where a purely shear-dominated flow was reproduced. Tampieri *et al.* (2000) also suggested that lower values of α should correspond to the purely convective case.

For comparison data corresponding to case 0 are also shown in figure 10. It can be observed that they agree quite well with the law (3.5).

In a subsequent analysis Maurizi (2006) demonstrated that values above the curve given by equation (3.5) correspond to damping terms for the turbulent kinetic energy, which proves that a higher rotation speed increases the turbulent flow stability.

Concerning the QN approximation, figure 10 shows that it fails for cases 1A and 1B, while it can be considered acceptable for case 0, which is characterazed by a slower rotation speed. In fact, the kurtosis approaches the value of 3 when the skewness is close to zero as prescribed by the QN approximation $Ku = 3(S^2 + 1)$.

3.3. *Surface effect*

The last comparison we performed is between two experiments carried out over different surfaces. In the first one the wall surface was smooth while the second one was characterized by a transition from a rough to a smooth surface, as described in § 2. The main parameters are summarized in table 3.

Looking at figure 11, where the profiles of the measured mean velocity are shown, it can be observed that the smooth case 2A exhibits a simple logarithmic behaviour, whereas the rough-to-smooth profiles clearly show the fine structure due to the evolution of an internal boundary layer.

The profile closest to the transition presents the typical behaviour of a boundary layer above surface roughness, showing a deeper shear layer and hence a larger u_τ. The profiles farther from transition accelerate over the smooth surface in the lower layers in order to reach the new equlibrium state, which exhibits a trend similar to that of the smooth case 2A and a decreasing stress u_τ (see table 3).

This suggests that the flow is not horizontally homogeneous because the roughness elements placed upstream generate instabilities which, advected by the flow, propagate downstream.

SOM profiles of the developed turbulence in the boundary layer (normalized with u_τ^2) are depicted in figure 12(*a*–*d*). $\langle u'v' \rangle$ and $\langle u'^2 \rangle$ show that the further the flow

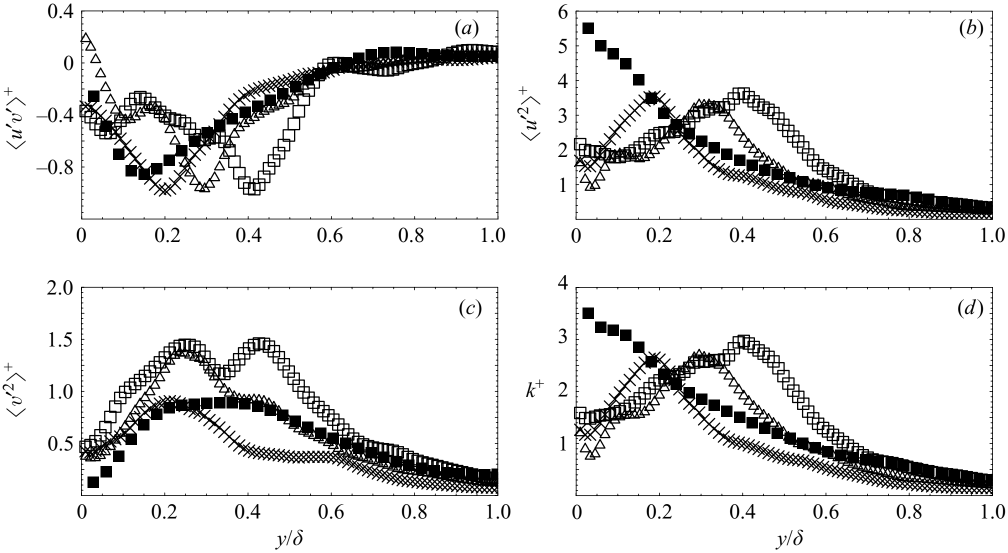

FIGURE 12. Case 2: normalized SOMs vs. normalized wall distance. ■, case 2A; ×, case 2B (0.5 h_r); △, case 2B (3.5 h_r); □, case 2B (6.6 h_r).

travels over the smooth surface, the further the wall distance of their maximum value increases. This is about 0.2δ, 0.3δ and 0.4δ for the profiles taken at distances from the measurement field edge of 0.5 h_r, 3.5 h_r and 6.6 h_r respectively, giving rise to the following non-dimensional relationship for the ratio of the increment of the moment maximum distance from the wall Δy to the downstream distance increment Δx:

$$\frac{\Delta y}{\Delta x} = \frac{1}{30}\frac{\delta}{h_r}. \tag{3.6}$$

The distance of the maximum from the wall can be considered to be the depth of an internal boundary layer which grows with the downwind distance as shown by LES performed by Glendening & Lin (2002).

TOMs (normalized with u_τ^3) for both smooth and rough-to-smooth cases (2A and 2B in table 3) are reproduced in figure 13(*a–d*). Roughness elements in case 2B act as a trigger for the large turbulent structures which increase the non-local transport inside the boundary layer, as it is confirmed by TOM profiles downstream of the roughness elements. While the closest profiles (0.5h_r) are similar to the smooth case, the farthest ones (3.5 h_r and 6.6 h_r) are larger than in the smooth case.

The TOMs measured over a smooth surface show a regular profile with a definite sign and, as already mentioned, their behaviour is similar to that obtained in numerical simulations using both LES (Moeng & Sullivan 1994) and Reynolds stress averaged models (Ferrero 2005). On the contrary, the profiles corresponding to the case of rough-to-smooth transition alternate in sign crossing zero at about 2 h_r.

The boundary layer splitting into two parts with different turbulent moments behaviours is typical of the turbulence generated by a canopy (Raupach, Coppin & Legg 1986) where the roughness element height is an essential parameter for the flow description.

In figure 14 the FOMs (normalized with u_τ^4) obtained in experiment 2B are shown. For comparison the QN approximation results are also depicted. The FOMs profiles closest to the transition from the rough to the smooth surface have larger values than

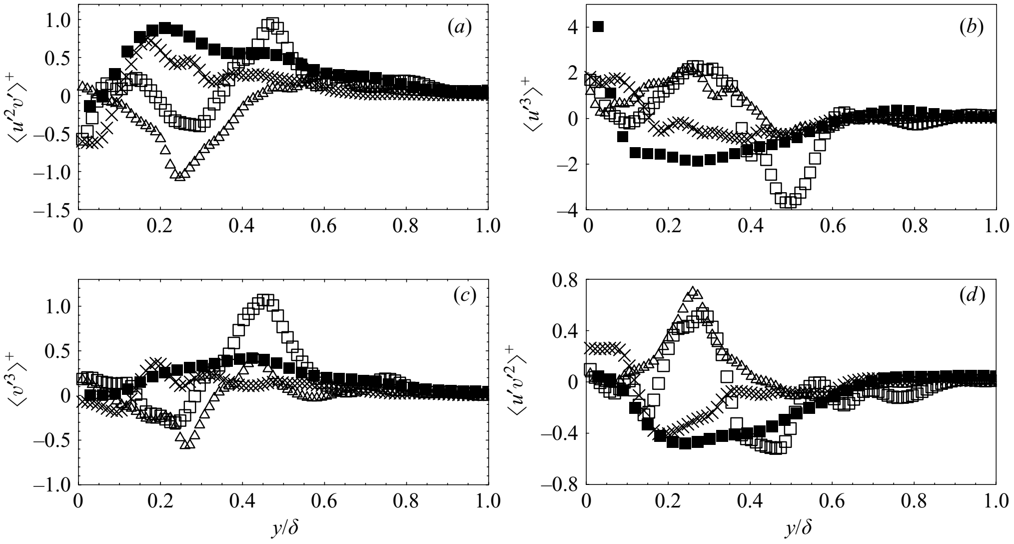

FIGURE 13. Case 2: normalized TOMs vs. normalized wall distance. ■, case 2A; ×, case 2B (0.5 h_r); △, case 2B (3.5 h_r); □, case 2B (6.6 h_r).

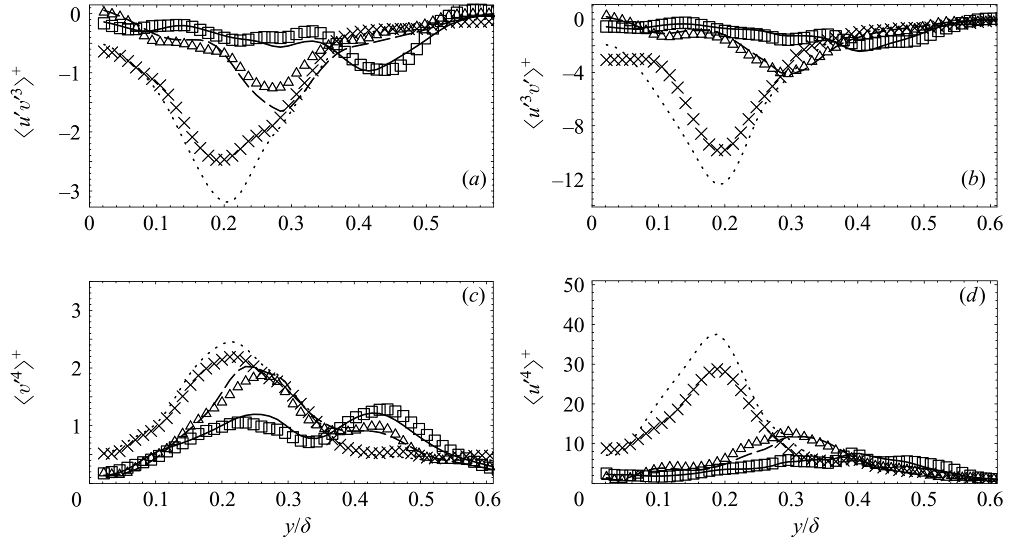

FIGURE 14. Case 2: normalized FOMs vs. normalized wall distance. ×, case 2B (0.5 h_r); △, case 2B (3.5 h_r); □, case 2B (6.6 h_r). The dotted, dashed and solid lines are case 2B (0.5 h_r), (3.5 h_r) and (6.6 h_r) QN approximation data respectively.

those at greater distances. The QN hypothesis seems to be a good approximation of the measured FOM only in the case of the farthest profiles, while it fails when the profile closest to the transition is considered.

Figure 15 presents the kurtosis as a function of the skewness in the 2A and 2B cases. It can be observed that these values are almost entirely below the curve given by equation (3.5). Following Maurizi (2006), these results, showing that most of the values are below the $Ku = 3$ line, indicate that the flow is unstable, as expected due to the presence of high roughness elements upstream. Even though the discrepancies

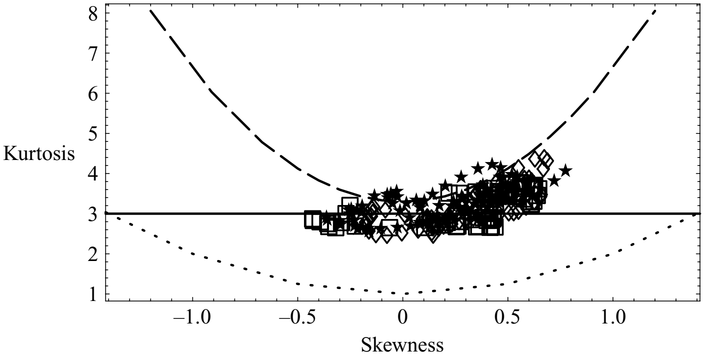

FIGURE 15. Kurtosis as a function of the skewness for cases over the rough-to-smooth surface. □, case 2B (0.5 h_r); ⋆, case 2B (3.5 h_r); ◇, case 2B (6.6 h_r). Dashed line: $Ku = 3.3(S^2 + 1)$, solid line: $Ku = 3$; dotted line: $Ku = S^2 + 1$.

are not as large as in cases 1A and 1B the QN hypothesis seems to fail in this case as well.

As observed by Cheng *et al.* (2005) the departure from the QN approximation can be interpreted as related to the non-local nature of the turbulent flow.

4. Conclusions

The results of experiments reproducing a shear-driven boundary layer in a rotating tank are presented. Different flows were generated by changing the tank rotation speed in order to observe Coriolis force effects on the boundary layer. Two kinds of bottom surfaces were considered: an evenly uniform smooth surface and a transition from a rough to a smooth wall. The boundary layer and its inner fine structure, developed in all the experiments, were measured and analysed.

The main boundary layer parameters were estimated in order to properly normalize the measured variables and to evaluate the Reynolds and the Rossby numbers.

First, the consistency between the experimental results and results from the boundary layer theory was verified by comparing our measured data with the log-law and a large-eddy simulation. To this end, a first case with relatively small rotation velocity was chosen. The results agree with theoretical and numerical model predictions both for the mean flow and the higher-order turbulence moments.

Then the effect of the rotation was investigated by comparing two experiments characterized by different rotation periods. The turbulence moments show larger values in a layer near the wall, which becomes thinner as the tank rotation period decreases. Thus, the higher rotation speed prevents the turbulent transport developing outside a layer very close to the wall.

The comparison of the experiments carried out over different kinds of surfaces show that the rough-to-smooth transition generates, as expected, an internal boundary layer growing with the distance. In particular, the height of the second-order moment maximum also increases with the distance and the third-order moment profiles show a behaviour similar to that found in a canopy. TOMs also indicate the presence of a large non-local transport triggered by the roughness elements.

Finally, the analysis of the fourth-order moments demonstrates that measured profiles support the QN hypothesis both over smooth and rough-to-smooth surfaces (except for the profile closest to the transition), but it fails for flows with greater rotation speed. Furthermore the values of the kurtosis plotted versus the skewness suggest that the rotation acts on the flow as sink of turbulence making the turbulent layer shallower and more stable. On the contrary, the roughness elements placed upstream trigger instabilities propagating downstream over the smooth surface.

The authors wish to thank Dr R. Forza for his skilful technical support during the experimental runs and for maintaining and up-grading the efficiency and reliability of the experimental apparatus.

REFERENCES

Adrian, R. J., Meinhart, C. D. & Tomkins, C. D. 2000 Vortex organization in the outer region of the turbulent boundary layer. *J. Fluid Mech.* **422**, 1–54.

Bendat, J. S. & Piersol, A. G. 1986 *Random Data: Analysis and Measurement Procedures, 2nd Edition*, 2nd edn. John Wiley & Sons.

Bernero, S. & Fiedler, H. E. 2000 Application of particle image velocimetry and a proper orthogonal decomposition to the study of jet in a counterflow. *Exps. Fluids (supp.)* pp. S274–S281.

Bidokhti, A. A. & Tritton, D. J. 1992 The structure of a turbulent free shear leyer in a rotating fluid. *J. Fluid Mech.* **241**, 469–502.

Canuto, V. M. 1992 Turbulent convection with overshooting: Reynolds stress approach. *Astrophys. J.* **392**, 218–318.

Cheng, Y., Canuto, V. M. & Howard, A. M. 2005 Nonlocal convective pbl model based on third- and fourth-order moments. *J. Atmos. Sci.* **62**, 2189–2204.

Coleman, G. N., Ferziger, J. H. & Spalart, P. R. 1990 A numerical study of the turbulent ekman layer. *J. Fluid Mech.* **213**, 313–348.

Drobinski, P., Carlotti, P., Newsom, R. K., Banta, R. M., Foster, R. C. & Redelsperger, J. L. 2004 The structure of the near-neutral surface layer. *J. Atmos. Sci.* **61**, 699–714.

Drobinski, P., Carlotti, P., Redelsperger, J. L., Banta, R. M. & Newsom, R. K. 2007 Numerical and experimental investigation of the neutral surface layer. *J. Atmos. Sci.* **64**, 137–156.

Ferrero, E. 2005 Third order moments for shear driven boundary layers. *Boundary Layer Metary.* **116**, 461–466.

Ferrero, E., Longhetto, A., Montabone, L., Mortarini, L., Manfrin, M., Sommeria, J., Didelle, H., Giraud, C. & Rizza, U. 2005 Physical simulation of neutral boundary layer in rotating tank. *Il Nuovo Cimento* **28 C**, 1–17.

Ferrero, E. & Racca, M. 2004 The role of the nonlocal transport in modeling the shear-driven atmospheric boundary layer. *J. Atmos. Sci.* **61**, 1434–1445.

Fincham, A. M. & Spedding, G. R. 1997 Low-cost, high resolution dpiv for measurement in turbulent fluid flows. *Exps. Fluids* **23**, 449–462.

Glendening, J. W. & Lin, C.-L. 2002 Large eddy simulation of internal boundary layers created by a change in surface roughness. *J. Atmos. Sci.* **59**, 1697–1711.

Gluhovsky, A. & Agee, E. M. 1994 A definitive approach to turbulence statistical studies in planetary boundary layers. *J. Atmos. Sci.* **51**, 1682–1690.

Grant, A. L. M. 1986 Observations of boundary layer structure made during the 1981 kontur experiment. *Q. J. R. Met. Soc.* **112**, 825–841.

Grant, A. L. M. 1992 The structure of turbulence in the near-neutral atmospheric boundary layer. *J. Atmos. Sci.* **49**, 226–239.

Gryanik, V. M. & Hartmann, J. 2005 A refinement of the millionshchikov quasi-normality hypothesis for convective boundary layer turbulence. *J. Atmos. Sci.* **62**, 2632–2638.

Hanjalic, K. & Launder, B. E. 1972 A reynolds stress model of turbulence and its application to thin shear flows. *J. Fluid Mech.* **52**, 609–638.

Hanjalic, K. & Launder, B. E. 1976 Contribution towards a reynolds-stress closure for low-reynolds-number turbulence. *J. Fluid Mech.* **74**, 593–610.

Hartmann, J., Albers, F., Argentini, S., Bochert, A., Bonate, U., Cohrs, W., Conidi, A., Freese, D., Georgiadis, T., Ippoliti, A., Kaleschke, L., Lupkes, C., Maixner, U., Mastrantonio, G., Ravegnani, F., Reuter, A., Trivellone, G. & Viola, A. 1999 Arctic radiation and turbulence interaction study (artist). reports on polar research. *Tech. Rep.* 305. Alfred Wegener Institute for Polar and Marine Research, Bremerhaven.

Hunt, J. C. R. & Carlotti, P. 2001 Statistical structure at the wall of the high reynolds number turbulent boundary layer. *Flow, Turbulence, Combust.* **66**, 453–475.

Khurshudyan, L., Snyder, L. H. & Nekrasov, I. V. 1981 Flow and dispersion of pollutants over two- dimensional hills: Summary report on joint soviet-american study. *Rep. No. EPA-600/4-81-067*, p. 131.

Lenschow, D. H., Mann, J. & Kristensen, L. 1994 How long is long enough when measuring fluxes and other turbulence statistics? *J. Atmos. Ocean. Technol.* **11**, 661–673.

Lesieur, M. 1997 *Turbulence in Fluids*. Kluwer.

Lin, C. L., McWilliams, J. C., Moeng, C. H. & Sullivan, P. P. 1996 Coherent structures in a neutrally-stratified planetary boundary layer. *Phys. Fluids* **8**, 2626–2639.

Losch, M. 2004 On the validity of the millionshchikov quasi-normality hypothesis for open-ocean deep convection. *Geophys. Res. Lett.* **31**, L23301.

Mason, P. J. & Sykes, R. I. 1980 A two dimensional numerical study of horizontal roll vortices in the neutral atmospheric boundary layer. *Q. J. R. Met. Soc.* **106**, 351–366.

Mason, P. J. & Thomson, D. J. 1987 Large-eddy simulation of the neutral-static-stability planetary boundary layer. *Q. J. R. Met. Soc.* **113**, 413–443.

Maurizi, A. 2006 On the dependence of third- and fourth-order moments on stability in the turbulent boundary layer. *Nonlin. Proc. Geophys.* **13**, 119–123.

Millikan, C. M. 1938 A critical discussion of turbulent flows in channels and circular tubes. *Proc. Fifth International Congress on Applied Mechanics*, pp. 386–392.

Moeng, C.-H & Sullivan, P. P. 1994 A comparison of shear and buoyancy driven planetary boundary layer flow. *J. Atmos. Sci.* **51**, 999–1022.

Monin, A. & Yaglom, A. 1971 *Statistical Fluid Mechanics*, vol. 1. MIT Press.

Nicholls, S. & Readings, C. J. 1979 Aircraft observations of the structure of the lower boundary layer over the sea. *Q. J. R. Met. Soc.* **105**, 785–802.

Ohba, R., Hara, T., Nakamura, S., Ohya, Y. & Uchida, T. 2002 Gas diffusion over an isolated hill under neutral, stable and unstable conditions. *Atmos. Environ* **36**, 5697–5707.

Pedlosky, J. 1987 *Geophysical Fluid Dynamics*. Springer.

Prasad, A. K., Adrian, R. J., Landreth, C. C. & Offutt, P. W. 1992 Effect of resolution on the speed and accuracy of particle image velocimetry interrogations. *Exps. Fluids* **13**, 105–116.

Qian, M. W., Longhetto, A., Cassardo, C., Giraud, C., Hong, Z. X., Luo, W. D. & Zhao, Y. J. 2000 Heat energy balance in the convective atmospheric boundary layer at Xianghe (Beijing area), China. *J. Atmos. Sci.* **57**, 3881–3890.

Raffel, M., Willert, C. E. & Kompenhans, J. 1998 *Particle Image Velocimetry, a Practical Guide*. Springer.

Rao, K. S., Wyngaard, J. C. & Coté, O. R. 1973 The structure of the two-dimensional internal boundary layer over a sudden change of surface roughness. *J. Atmos. Sci.* **11**, 738–746.

Raupach, M. R., Coppin, P. A. & Legg, B. J. 1986 Experiments on scalar dispersion within a plant canopy, part i: the turbulence structure. *Boundary Layer Met.* **35**, 21–52.

Rizza, U., Gioia, G., Mangia, C. & Marra, G. P. 2003 Development of a grid-dispersion model in a large-eddy-simulation-generated pbl. *Il Nuovo Cimento 26C* **3**, 297–309.

Tampieri, F., Maurizi, A. & Alberghi, S. 2000 Lagrangian models of turbulent dispersion in the atmospheric boundary layer. *Proc. Ingegneria del Vento in Italia 2000*, pp. 37–50.

Tarbouriech, L., Didelle, H. & Renouard, D. 1997 Time-series *piv* measurements in a very large rotating tank. *Exps. Fluids* **23**, 438–440.

Tritton, D. J. 1988 *Physical Fluid Dynamics*. Oxford University Press.

Zanoun, E., Durst, F. & Nagib, H. 2003 Evaluating the law of the wall in two-dimensional fully developed turbulent channel flows. *Phys. Fluids* **15**, 3079–3089.

Zeman, O. 1981 Progress in the modeling of planetary boundary-layers. *Annu. Rev. Fluid Mech.* **13**, 253–272.

Zilitinkevich, S. S., Gryanik, V. M., Lykossov, V. N. & Mironov, D. V. 1999 Third-order transport and nonlocal turbulence closures for convective boundary layers. *J. Atmos. Sci.* **56**, 3463–3477.